



저작자표시-비영리-변경금지 2.0 대한민국

이용자는 아래의 조건을 따르는 경우에 한하여 자유롭게

- 이 저작물을 복제, 배포, 전송, 전시, 공연 및 방송할 수 있습니다.

다음과 같은 조건을 따라야 합니다:



저작자표시. 귀하는 원저작자를 표시하여야 합니다.



비영리. 귀하는 이 저작물을 영리 목적으로 이용할 수 없습니다.



변경금지. 귀하는 이 저작물을 개작, 변형 또는 가공할 수 없습니다.

- 귀하는, 이 저작물의 재이용이나 배포의 경우, 이 저작물에 적용된 이용허락조건을 명확하게 나타내어야 합니다.
- 저작권자로부터 별도의 허가를 받으면 이러한 조건들은 적용되지 않습니다.

저작권법에 따른 이용자의 권리는 위의 내용에 의하여 영향을 받지 않습니다.

이것은 [이용허락규약\(Legal Code\)](#)을 이해하기 쉽게 요약한 것입니다.

[Disclaimer](#)

Master's Thesis of Mechanical Engineering

Non-resonant Barrier-Penetrating Ultrasonic Metamaterial

비공진 장애물 투과 초음파 메타물질

August 2023

Graduate School of Mechanical Engineering
Seoul National University

Gihyun Kim

Non-resonant Barrier-Penetrating Ultrasonic Metamaterial

Advisor Yoon Young Kim

Submitting a master's thesis of
Mechanical Engineering

April 2023

Graduate School of Mechanical Engineering
Seoul National University

Gihyun Kim

Confirming the master's thesis written by
Gihyun Kim

June 2023

Chair	<u>Byung Dong Yoon</u>	(Seal)
Vice Chair	<u>Yoon Young Kim</u>	(Seal)
Examiner	<u>Do-Nyun Kim</u>	(Seal)

Abstract

Non-resonant Barrier-Penetrating Ultrasonic Metamaterial

Gihyun Kim

Department of Mechanical Engineering

The Graduate School

Seoul National University

The intrinsic reduction in wave transmission caused by the reflection when a barrier intercepts the propagation path has long constrained the application of elastic ultrasound. This study presents a pioneering metamaterial design to enable the full transmission of elastic ultrasound waves across barriers. Through mathematical analysis and physical interpretation of the phenomenon of fully transmitting waves across the barrier, we confirm the possibility of implementing this phenomenon through the design of a non-resonant metamaterial. We also ascertain and explain the theoretical prerequisites a non-resonant metamaterial designed for barrier penetration should fulfill. This understanding subsequently guides the design of a metamaterial that meets these stipulated conditions. The efficiency of the proposed metamaterial is substantiated both numerically via finite element method-based simulations and experimentally via ultrasonic experiments in the aluminum–water–aluminum system. Our findings open a vista for

advancements in fields such as non-destructive testing across barriers and in the development of medical devices, including brain ultrasound systems, underscoring the pragmatic implications of our research.

Keyword : Ultrasonic waves, Elastic metamaterials, Barrier-penetrating full transmission, Fabry-Perot resonance, Impedance matching

Student Number : 2021-23094

Table of Contents

Chapter 1. Introduction	1
1.1 Research motivation	1
1.2 Purpose of research	3
Chapter 2. Theoretical Background.....	7
2.1 Underlying physics of barrier penetration	7
2.2 Material properties for barrier penetration	11
Chapter 3. Design of barrier penetrating metamaterials	19
3.1 Metamaterial modeling	19
3.2 Optimization formulation and results	21
Chapter 4. Validation.....	27
4.1 FEM simulation results and analysis	27
4.2 Experimental validation	29
Chapter 5. Conclusion	40
 Bibliography	 41
 Abstract in Korean.....	 45

Chapter 1. Introduction

1.1. Research motivation

The utilization of metamaterials for wave control has seen increasing implementation in diverse applications, ranging from lenses and antennas to non-destructive testing and medical devices [1–11]. The transmission of high-energy waves to target points is an essential aspect of these wave-based applications, whether electromagnetic or elastic waves. Elastic waves have been attracting attention because they are harmless to the human body, portable, easy to use, and affordable. They are used in a variety of applications, such as measuring the flow inside pipes using ultrasound [12–14], detecting defects inside structures made of materials difficult for electromagnetic waves to penetrate [15–17], and in medical treatment and diagnosis [18–21]. These technologies utilizing elastic waves are often used for inspection and diagnosis purposes, but a fundamental problem limits the application of existing technologies.

Reflected waves generated from a highly impedance-mismatched barrier cause a significant reduction in the transmission of ultrasound through the barrier. This reduction in transmittance has been a persistent limitation of the efficacy of ultrasonic equipment. Figure 1.1(a) is a schematic that well illustrates this phenomenon, showing that wave reflection can be a significant constraint on performance when a barrier is located along the wave path.

Various research has been carried out to compensate for such losses and preserve the functionality of ultrasonic equipment. Research on impedance matching aims to overcome impedance mismatches at the boundary of ultrasound generators and transmit more energy across the interfaces of different media. In ultrasound flowmeters, longitudinal-to-transverse wave mode conversion technology has successfully been used to transmit much higher energy waves beyond barriers. In the case of transcranial ultrasound research, there are studies on signal processing to restore lost signals and maximize the focus of penetrated ultrasound energy. However, this research does not primarily aim to overcome barriers directly and fully preserve penetrating waves. Not only these circumventive techniques but also solutions that fundamentally overcome barriers and increase transmission rates have been discussed. The Fabry-Pérot resonance (FPR) has been generally used as a solution to this issue, although it only enables full penetration when the frequency-barrier thickness aligns with a particular value [22]. As an alternative, the employment of complementary material (CM) has been proposed as a means to theoretically cancel out the barrier, facilitating full ultrasound penetration devoid of any reflection [23]. However, the deployment of a complementary metamaterial layer (CML)s mandates the use of highly sensitive, locally resonant structures, which have proven challenging to actualize experimentally [24]. The use of these sensitive locally resonant structures in CML is to meet the negative phase change required conceptually for canceling out the barriers.

The sensitivity of locally resonant structures has prohibited experimental implementation by changing the local resonance frequency even with minute errors and losing its function. Some have also overcome lossy barriers using non-Hermitian CMM [25]. In the case of non-Hermitian systems, it seems more work is needed to utilize them in practical implementation as they use complex loss-gain systems. In recent years, there has been a surge of research focusing on applying non-resonant metamaterials for elastic ultrasonic wave control, aiming to overcome the constraints associated with locally resonant metamaterials [26–28].

There is a necessity for research on the physical phenomena that can fundamentally improve the efficiency of barrier penetration by adopting the benefits of such non-resonant systems and practical systems that can realize these phenomena.

1.2. Purpose of Research

As shown in Figure 1.1 (b), our goal is to develop a system that suppresses unwanted reflections by inserting metamaterials in front of a barrier, thus achieving full wave penetration across the barrier. In this research, we propose non-locally resonant elastic metamaterials that facilitate the full transmission of elastic ultrasound waves through barriers, as shown in Figure 1.2. We establish the theoretical prerequisites for the properties of a metamaterial layer to enable full elastic wave penetration and actualize a metamaterial layer adhering to these prerequisites in the

form of a non-resonant elastic metamaterial bearing an X-shaped microstructure. Our investigation reveals that the employment of non-resonant elastic metamaterials with X-shaped microstructures not only enables full ultrasound penetration through high impedance mismatched barriers but also demonstrates augmented robustness and broader bandwidth compared to those actualized using locally resonant structures. The effectiveness of the proposed metamaterials is validated through finite element method (FEM) simulations and experiments.

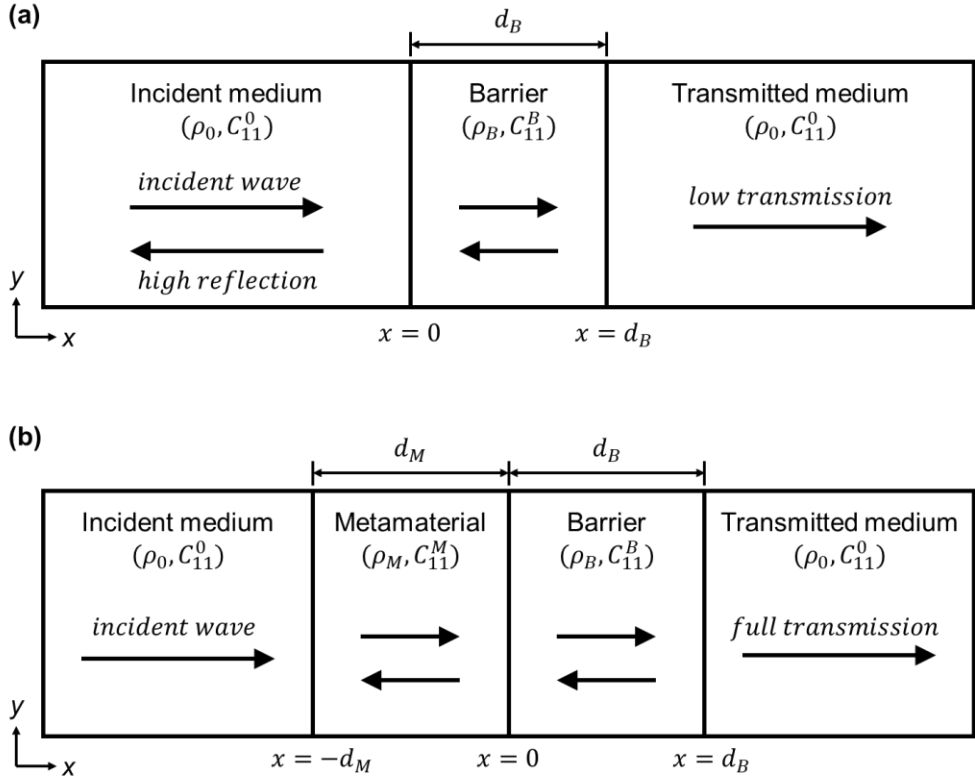


Fig. 1.1. Schematics of wave propagation in the presence of a barrier (a) without and (b) with metamaterial layer

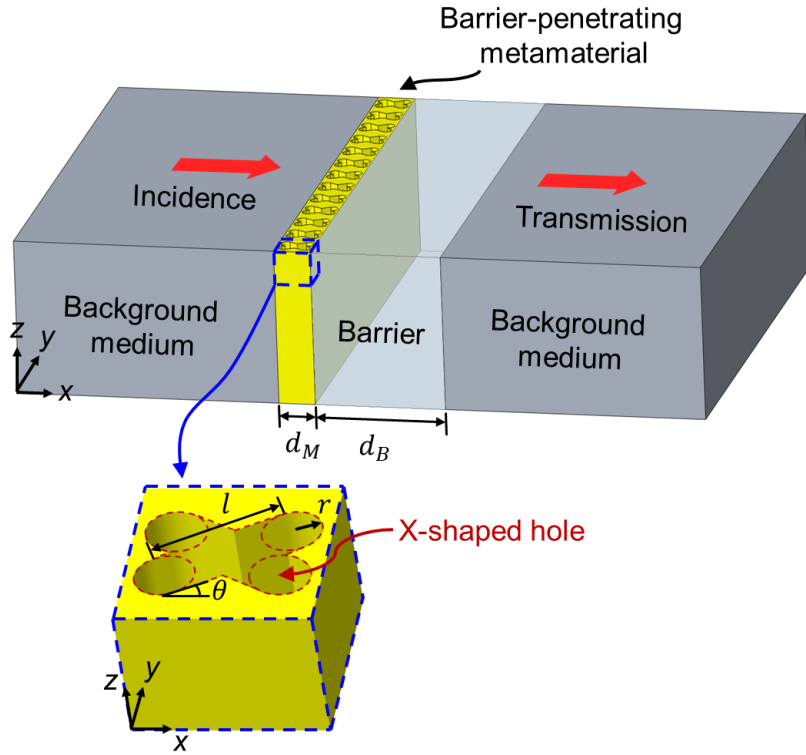


Fig. 1.2. Schematics of the non-resonant barrier penetrating ultrasonic metamaterial.

Chapter 2. Theoretical background

2.1. Underlying physics of barrier penetration

In this chapter, we explore the fundamental physical phenomena that enable barrier penetration. Figure 1.1 shows a basic schematic of the physical phenomena of barrier penetration. The material of the barrier can exist in various states, regardless of its physical phase. Notably, under highly impedance mismatch conditions where there's a significant difference between the impedance of the background medium and the barrier, the transmission rate of the wave can be diminished extremely low. We can surmise that a metamaterial layer might require different physical properties depending on the characteristics of a barrier. We analyze the phenomena that overcome the various factors that hinder barrier penetration and allow the wave to fully transmit across the barrier. In this analysis process, we define the wave used as a typical elastic wave and consider longitudinal waves propagating within elastic media.

First, we express the waves propagating in the metamaterial layer and barrier as a transfer matrix. When establishing the transfer matrix, we need to consider the field continuity for the boundary condition, which can be expressed as Equation (2.1), at interfaces such as $x = -d_M$, $x = 0$, and $x = d_B$ in Figure 1.1 where the composing materials differ.

$$\begin{bmatrix} v_L \\ F_L \end{bmatrix} = \begin{bmatrix} v_R \\ F_R \end{bmatrix} \quad (2.1)$$

where v denotes velocity, F denotes force, subscript L denotes the left side of the boundary condition, and subscript R denotes the right side of the boundary condition.

Taking into account the wave propagation inside each layer, the transfer matrix for the barrier and metamaterial can be expressed as Equations (2.2) and (2.3).

$$\mathbf{T}_M = \mathbf{M}_M \mathbf{N}_M \mathbf{M}_M^{-1} \quad (2.2)$$

$$\mathbf{T}_B = \mathbf{M}_B \mathbf{N}_B \mathbf{M}_B^{-1} \quad (2.3)$$

With

$$\begin{aligned} \mathbf{M}_M &= \begin{bmatrix} 1 & 1 \\ -Z_M & Z_M \end{bmatrix} \\ \mathbf{M}_B &= \begin{bmatrix} 1 & 1 \\ -Z_B & Z_B \end{bmatrix} \\ \mathbf{N}_M &= \begin{bmatrix} e^{-ik_M d_M} & 0 \\ 0 & e^{ik_M d_M} \end{bmatrix} \\ \mathbf{N}_B &= \begin{bmatrix} e^{-ik_B d_B} & 0 \\ 0 & e^{ik_B d_B} \end{bmatrix} \end{aligned}$$

where Z denotes the mechanical impedance of materials, k denotes the wavenumber, d denotes the length of each layer that wave travels, subscript M denotes the metamaterial, and subscript B denotes the barrier.

We implement a scattering matrix method, which is an efficient tool to evaluate the dynamic harmonic responses and thus the wave characteristics of the whole wave propagating system [29]. The wave propagating system using scattering parameters can be

expressed as Equation (2.4)

$$\begin{bmatrix} T e^{-ik_{BG}d} \\ 0 \end{bmatrix} = \begin{bmatrix} S_{11} & S_{12} \\ S_{21} & S_{22} \end{bmatrix} \begin{bmatrix} 1 \\ R \end{bmatrix} = \mathbf{S} \begin{bmatrix} 1 \\ R \end{bmatrix} \quad (2.4)$$

where T denotes the transmission coefficient, and R denotes the reflection coefficient.

A scattering matrix \mathbf{S} for elastic waves is defined in terms of the relationships between the incoming and scattered wave fields. The scattering matrix using a transfer matrix and considering boundary conditions with background medium can be expressed as Equation (2.5).

$$\mathbf{S} = \mathbf{M}_{BG}^{-1} \mathbf{T}_M \mathbf{T}_B \mathbf{M}_{BG} \quad (2.5)$$

$$\text{with } \mathbf{M}_{BG} = \begin{bmatrix} 1 & 1 \\ -Z_{BG} & Z_{BG} \end{bmatrix}$$

where subscript BG denotes the background medium.

By substituting Equations (2.2) and (2.3) into Equation (2.5), we are able to derive individual scattering parameters (S-parameters), which are expressed in terms of the constitutive variables of the metamaterials, barriers, and background materials.

From Equation (2.4), we can calculate both the reflection and the transmission coefficients. Considering the non-reflective condition to these coefficients, we can derive the requisite physical conditions for achieving full transmission as

$$\sin(d_B k_B) \sin(d_L k_L) \left(\frac{Z_B}{Z_L} - \frac{Z_L}{Z_B} \right) = 0 \quad (2.6)$$

$$\sin(d_B k_B) \cos(d_L k_L) \left(\frac{Z_{BG}}{Z_B} - \frac{Z_B}{Z_{BG}} \right) + \cos(d_B k_B) \sin(d_L k_L) \left(\frac{Z_{BG}}{Z_L} - \frac{Z_L}{Z_{BG}} \right) = 0$$

(2.7)

These equations are identically satisfied if the following relations hold two conditions expressed as Equations (2.8) and (2.9).

$$Z_M = Z_B \quad (2.8)$$

$$k_M d_M + k_L d_L = n\pi \quad (n: \text{integer}) \quad (2.9)$$

These prescribed physical conditions describe the mechanisms of barrier penetration. To facilitate full transmission through a barrier located between background media, the metamaterial should have the "same impedance" concurrent with the barrier. In contrast, the summative phase changes associated with both the metamaterial and the barrier must be a "multiple of π ". This suggests that the metamaterial and the barrier must emulate the dynamics of a single entity executing Fabry–Pérot resonance.

In a previous study using CML, they dealt with the case where $n=0$ in Equation (2.9). In this study, we consider the $n = \text{positive integer}$ case to circumvent the implementation of negative properties that led to limitations in the previous study. Here, the analysis implies that the barrier transmission phenomenon can be realized not only from layers with negative phase change, which is required in conventional CM but also from layers with positive phase change. Therefore, it demonstrates the possibility of full barrier penetration by designing metamaterials that satisfy properties with positive phase changes.

2.2. Material properties for barrier penetration

The metamaterial, situated in front of the barrier, enacts the previously delineated physics, ameliorating the issue of diminished transmittance consequential to a high impedance mismatched barrier. The properties of metamaterials can be determined when the material comprising the barrier and the background material is specified. We assume a barrier and background material to determine the material properties that a metamaterial layer should have in a practical barrier transmission situation. In this case, each component material is a homogeneous and isotropic material without any scattering substance, and the frequency is considered to be 100kHz.

Without loss of generality, we have defined the background material and the barrier as aluminum ($\rho = 2700 \text{ [kg/m}^3\text{]}$, $C_{11} = 102.234 \text{ [GPa]}$) and water ($\rho = 997 \text{ [kg/m}^3\text{]}$, $c = 1500 \text{ [m/s]}$), respectively. The reason for choosing these materials is to highlight the effectiveness of barrier-penetrating with a non-resonant metamaterial layer by creating an extreme impedance difference. In addition, the degradation of transmission efficiency at solid-fluid interfaces is a challenging problem, yet it often occurs in real-world cases [30–32]. The impedance difference between the background medium and the barrier in the case assumed in this paper is about 11 times, which is caused by the difference in wave propagation velocity and density difference resulting from the difference in material properties of metallic solid and fluid. The

barrier thickness ($d_B = 33.75\text{mm}$) was defined at the anti-FPR length to block wave propagation beyond it effectively. As shown in Figure 2.1, the wave penetration efficiency before the insertion of the metamaterial layer in this high impedance mismatch system is very low, at about 3–4%.

With all predeterminants defined for the background material and barrier, we can determine the density and stiffness of the metamaterial required to implement the full penetration physics as shown in Equations (2.10) and (2.11), respectively.

$$\rho_M = Z_M k_M / \omega \quad (2.10)$$

$$C_{11}^M = Z_M \omega / k_M \quad (2.11)$$

A noteworthy point to consider is the length (d_M) of the metamaterial in the direction of wave propagation. As delineated in Equations (2.10) and (2.11), given that the properties of the barrier (such as its thickness and material) are predetermined, the only free variable is the thickness of the metamaterial. Recalling Equation (2.9), it indicates that the wavenumber of the metamaterial layer (k_L) is functionally dependent on the thickness of the metamaterial. This suggests that the density and stiffness of the metamaterial for full barrier penetration can be expressed as a function of the metamaterial thickness, as shown in Figure 2.2. This indicates that the thickness of the metamaterial can be designed independently, and the prerequisites to be satisfied (ρ_M , C_{11}^M) vary congruently with the thickness of the metamaterial. This provides a rigid theoretical basis for the idea that we can freely set the

dimensions of the metamaterial we need. This topic will be further discussed in Chapter 3.1. Equation (2.9) also implies a relationship between the phase change inside the metamaterial and the metamaterial properties. Adjusting the value that determines the degree of phase change inside the metamaterial will change the properties that the metamaterial should have. Therefore, as shown in Figure 2.2, if the value that the metamaterial must meet for a particular phase change is extremely large or small at a certain length, it can provide efficient ways of avoiding it. In conclusion, the theoretically validated factors that can determine the properties of these metamaterials facilitate their design to an appropriate size and facile properties, representing controllable variables for designers. This signifies that they have the potential to enhance the feasibility of realizing a barrier full penetrating system.

To verify the effectiveness of our designed system, we performed a mathematical verification using the obtained properties. The effective properties of the metamaterial layer are $\rho = 534.107 \text{ [kg/m}^3\text{]}$, $C_{11} = 4.187 \text{ [Gpa]}$ and $d_M = 7 \text{ [mm]}$. Figure 2.3 mathematically compares the amplitude transmittance where the designed metamaterial is inserted and where there is only a barrier without metamaterial. A transmittance enhancement of about 559% in amplitude (about 3124% in energy) is observed when the metamaterial is in front of the barrier compared to no metamaterial. This aligns with the results of the effective property simulation using the FEM, as shown in Figure 2.4. Performing FEM by

replacing the metamaterial layer with the effective material, we found that the energy transmittance enhancement is about 3136%, with a very small error (0.384%) from the mathematical analysis. This confirms that the metamaterial material for barrier penetration we explored can work well in practice.

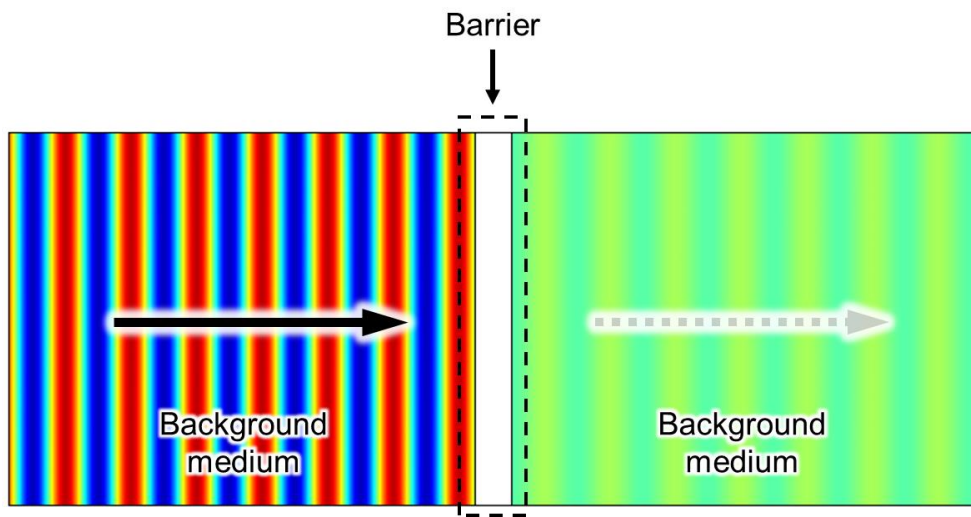


Fig. 2.1. Divergence field ($\nabla \cdot u$) of waves traveling towards a barrier in a high impedance mismatched system. The background medium is aluminum, and the barrier is water with a thickness of 33.75mm.

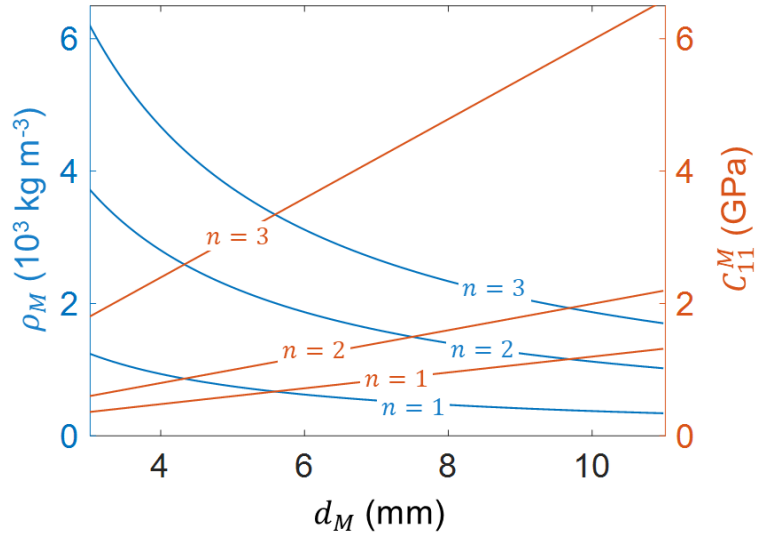


Fig. 2.2. Mass density and stiffness of the proposed metamaterials as a function of the thickness of the metamaterial.

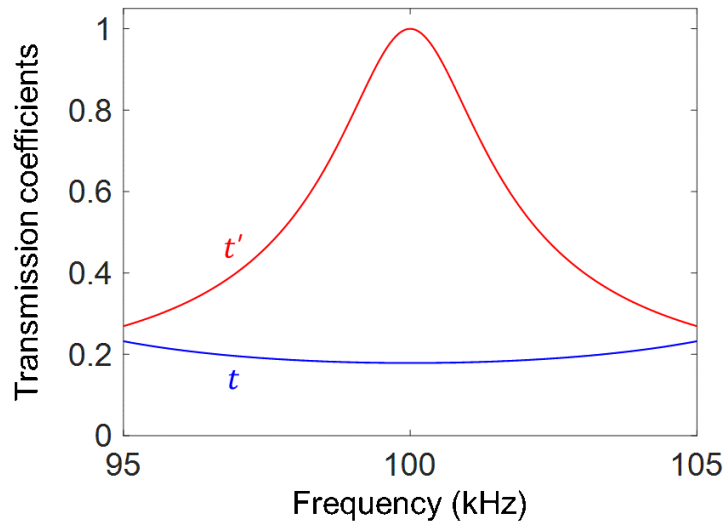


Fig. 2.3. Transmission coefficients without (blue) and with (red) the proposed metamaterial.

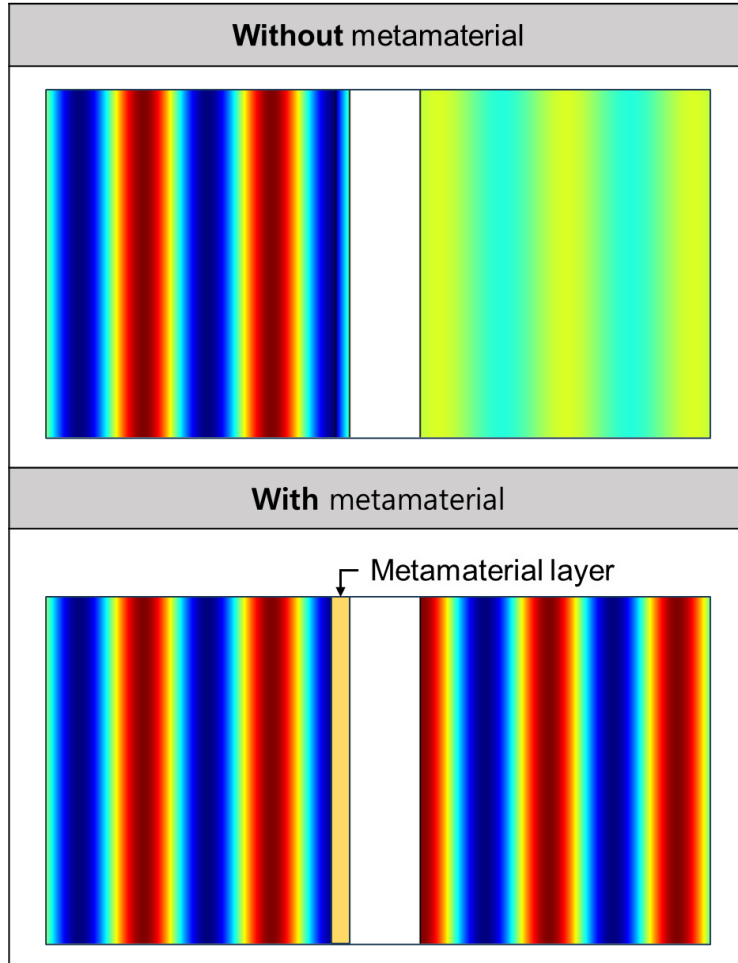


Fig. 2.4. Transmission efficiency comparison between a barrier-only case and a case using a metamaterial characterized by effective properties.

Chapter 3. Design of barrier penetrating metamaterials

3.1. Metamaterial modeling

As explored in the previous chapter, the properties required for complete barrier penetration can be satisfied by selecting appropriate materials and dimensional design. However, materials with these properties are unlikely to be found in nature. Therefore, we design a metamaterial with properties that enable barrier penetration at a specific length determined by the designer. This would be the most effective method as it allows for the precise implementation of more perfect barrier penetration properties in actual systems.

Metamaterials are artificially engineered materials that exhibit physical properties not observed in nature. They are composed of periodically arranged structures that can flexibly manipulate the behavior of waves based on their characteristics and the pattern of their arrangement [33]. Well-designed metamaterials can even be made to have their properties from a monolayer of structures alone, without the need for a repetitive arrangement of structures [34]. Based on these advantages, various studies dealing with waves have utilized metamaterials as a key tool. The design of these metamaterials is mainly done at the sub-wavelength scale because it makes metamaterials can interact with waves of a specific frequency and exhibit unique properties. Metamaterials with sub-wavelength unit structures do not allow waves to individually detect

each constituent element, thus allowing these structures to be perceived as a single continuous medium. This principle can confer characteristics not observed in natural materials, so this paper deals with the design of metamaterials at a sub-wavelength scale.

Another factor to consider in the design of metamaterial's structure is whether it is resonant or non-resonant. Metamaterials with a resonant structure can exhibit extraordinary properties by resonating at a specific frequency [5, 24]. This is because the structure of the metamaterial is designed to resonate at a specific frequency, which allows resonant metamaterials to maximize system response or to implement unique phenomena such as negative properties. But they have relatively large, complex unit structures and are highly sensitive to dimensional errors. In addition, they generally have a narrow bandwidth due to their resonant characteristics.

On the other hand, non-resonant metamaterials can be designed to have relatively simple and small unit structures. Although there are limitations in implementing special phenomena such as extreme or negative properties, they can design a relatively robust system against bandwidth and dimensional errors. In this paper, we take advantage of these non-resonant metamaterials by not requiring special situations such as negative or extreme properties. We chose the X-shaped unit structure, as shown in Figure 3.1, which has a simple geometry but allows us to realize various properties and features. Such structures have been used before in studies to control electromagnetic waves [35,36]. This

structure not only solves the disadvantages of locally resonant structures in the elastic wave regime but also enables barrier penetration of waves by satisfying the conditions expressed in Equations (2.8) and (2.9) by realizing the respective effective material properties described in Equations (2.10) and (2.11) with only a monolayer arrangement.

Fundamentally, the base material composing the metamaterial is not restricted and can be a variety of materials. In this study, we chose aluminum as the base material to form the metamaterial, considering the machinability of the structure and the ease of experimentation without loss of generality. The unit structure is processed to have voids in this base material. Through these mechanical processing methods, the metamaterial layer can be given unique properties at the target frequency we want.

3.2. Optimization formulation and results

By modeling the metamaterial's unit structure, we specify variables for the geometry and track the optimal values for these variables to embody the physics of barrier penetration. Computational simulation is used in the optimization process to obtain optimal values from the complex structure of the metamaterial and the responses that result from it. The geometry of the metamaterial determined through these optimization results will be an efficient structure for barrier penetration.

In the process of optimizing the metamaterial, all prerequisites

are the same as those discussed previously. The thickness of the metamaterial layer, which can be determined by the designer's intention or any actual needs, was randomly determined to be 5mm, 7mm, and 9mm, respectively, on a scale smaller than the wavelength to verify that the flexibility of the design is feasible. The dimension in the y -direction of the metamaterial is consistently retained at 7 mm. As shown in Figure 3.1, the geometric parameters in the X-shaped structure are defined as the line length l , the line edge radius r , and the angle orientation θ . The compact quantity of geometric variables in the unit cell structure significantly accelerates these design processes, offering an advantage concerning the requisite resources and temporal investment. The diverse metamaterials utilized in the case studies presented in this research were all predicated on an X-shaped unit cell structure with identical design parameters. The design process was conducted through optimization, employing the Method of Moving Asymptotes (MMA) algorithm. The design parameters were optimized by constructing an objective function to suppress reflections and unwanted modes. COMSOL Multiphysics 5.3 was used as the numerical solution tool for the optimization process.

The design of the metamaterial unit structure with each parameter value applied is shown in Figure 3.2. The parameter values of the optimized metamaterial are shown in Table 3.1, and the optimization results have successfully converged to full barrier penetration at all three target thicknesses. Although each has different values depending on the thickness, they prove that it is

possible to design with the same shape and parameters. This suggests that the proposed optimization method can be employed to design barrier-penetrating metamaterials of varying thicknesses, frequencies, and material compositions. This structural idiosyncrasy and parameterization ensure ample design flexibility, even under case study conditions featuring an impedance mismatch approximately 11 times. This significant deviation would ordinarily precipitate a substantial decline in wave transmission efficiency.

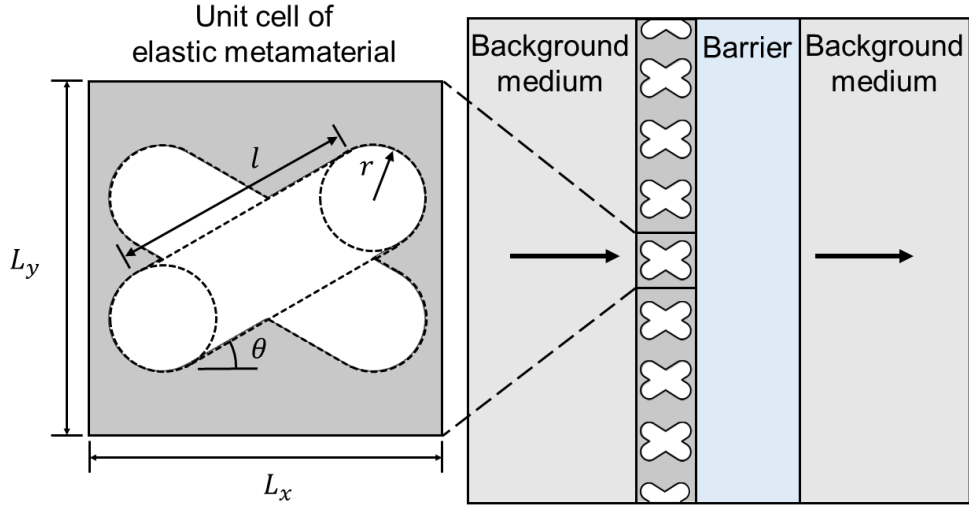


Fig. 3.1. Schematic of a metamaterial layer with a modeled X-shaped unit structure. The total of 5 unit cell decision variables is distinguished by three geometric parameters(r , l , θ) used for optimization and two predetermined geometric parameters(L_x , L_y).

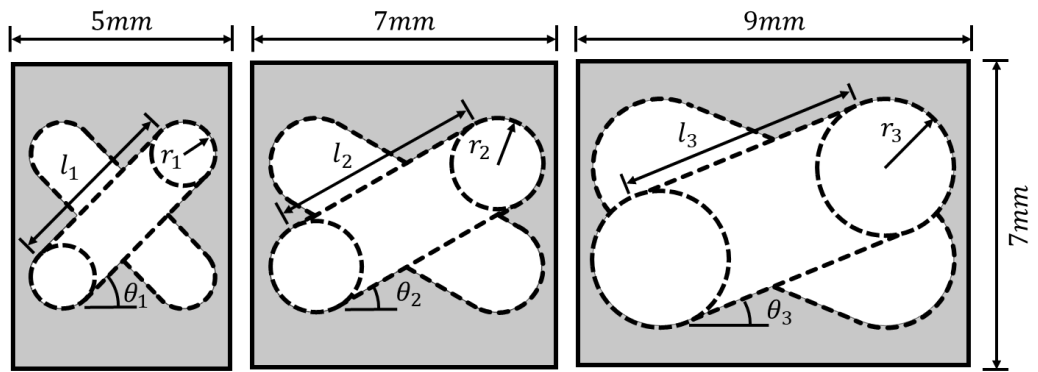


Fig. 3.2. Unit cell images of shape optimization results for different x-direction lengths.

$L_x = 5mm$	
$r_1 [mm]$	3.9626
$l_1 [mm]$	1.4581
$\theta_1 [deg]$	43.1678
$L_x = 7mm$	
$r_2 [mm]$	4.8684
$l_2 [mm]$	2.0879
$\theta_2 [deg]$	29.8540
$L_x = 9mm$	
$r_3 [mm]$	5.5610
$l_3 [mm]$	3.1500
$\theta_3 [deg]$	21.8978

Table 3.1. Optimized results of geometric parameters of the non-resonant barrier penetrating metamaterials.

Chapter 4. Validation

4.1. FEM simulation results and analysis

To confirm whether the design determined through shape optimization works well, we conducted verification through FEM simulation. COMSOL Multiphysics 5.3 was used as a numerical analysis tool for verification. Through this verification, we meticulously analyze the response characteristics of the metamaterial we have designed and confirm how well it implements the barrier penetration physics proposed in the theoretical analysis.

Here, we simulated a harmonic wave in the frequency domain. As shown in Figure 4.1. (a), the transmittance is observed to be less than 18% when only a barrier is present. However, upon the application of metamaterials of varying thicknesses, as shown in Figure 4.1. (b), (c) and (d) the transmittance surges beyond 99%. The only difference in the design process across each metamaterial is the thickness of the unit cell. This attests to the possibility of designing metamaterials with various thicknesses, each satisfying the essential physical conditions for achieving full transmittance, given identical design conditions. This infers a broad versatility, permitting design flexibility with respect to any thickness contingent on the particular requirements of a given situation. As shown in Figure 4.2, the frequency sweep of the designed metamaterials corresponds well with theoretical calculation and exhibits a consistent trend irrespective of thickness variations.

Figure 4.3 shows the response to the angle of incidence, suggesting that the engineered metamaterials possess substantial robustness with respect to variations in the angle of incidence. A high transmittance is observed across the entirety of the range of incident angles when the metamaterial is deployed, with a practically assured high transmittance within the typically utilized incident angle range of 0–30 degrees. These results demonstrate that the metamaterials consistently adhere to the antecedently deduced theoretical properties. Furthermore, they indicate that their performance can be sustained consistently, accommodating design flexibility to the thickness variations.

When determining the type of metamaterial, we chose a non-resonant structure to ensure the system's robustness. The robustness of such a system takes a role in suppressing factors that hindered experimental implementation in studies using CML [24]. To ensure that we have faithfully achieved this purpose, we compare the simulation results of the previous study with the simulation results of this study. Figure 4.4 shows the simulation results of barrier penetration at the target frequency when using CML and when using the non-resonant metamaterial. When the target frequency matches exactly, both CML and the proposed non-resonant metamaterial layer can observe that barrier penetration is successfully accomplished. Figure 4.5 shows the simulation results of barrier penetration when a wave of frequency deviating from the target frequency is incident when using CML and the non-resonant metamaterial. Even with a frequency offset of about 1kHz, CML

totally loses its function, whereas the proposed metamaterial was able to maintain over 80% transmission performance for amplitude. Figure 4.6 analyzes the frequency response corresponding to the frequency offset for these two metamaterials, showing the narrow bandwidth of the CML and the relatively wide bandwidth of the proposed non-resonant metamaterial. From these results, it can be confirmed that the proposed metamaterial has robustness against frequency by securing a wider bandwidth than CML, making practical implementation possible. This analysis can be extended to the incident angle and geometric error.

4.2. Experimental validation

We conducted wave transmission experiments to verify the full wave penetration across the barrier, using the conditions depicted in the numerical simulations. Among the various metamaterials designed, we chose a 7 mm thick metamaterial design. The metamaterial was precisely engineered onto a 150 mm thick aluminum block, as shown in Figure 4.7. Piezoceramic transducers, situated at both ends of the block with a cross-section of 150×150mm, functioned as emitters of the incident L-wave and detectors of the transmitted L-wave, respectively. The wave originating from the transmitter was incident vertically and, after penetrating the barrier (water), was measured at the sensor. These experimental systems are shown in Figure 4.7. Measurements were executed at the target frequency of 100 kHz and within a range of

± 5 kHz, progressing in intervals of 0.5 kHz. The data acquired, as shown in Figure 4.8, indicate that the application of a barrier-penetrating metamaterial amplified the maximum displacement amplitude of the transmitted L-wave at the target frequency by approximately 2.7 times relative to scenarios without the metamaterial. The frequency sweep response, shown in Figure 4.9, overlays the FEM simulation results with experimental data, considering the experimental conditions. The amplification ratio was calculated by dividing the amplitude observed with the metamaterial by the amplitude measured without it. As indicated in the simulation and experimental results, the amplification ratios exhibit a similar trend, implying the successful realization of the metamaterial designed according to the proposed theory. The experimental validation confirms that the fabricated metamaterials can substantially enhance the transmittance of waves penetrating barriers.

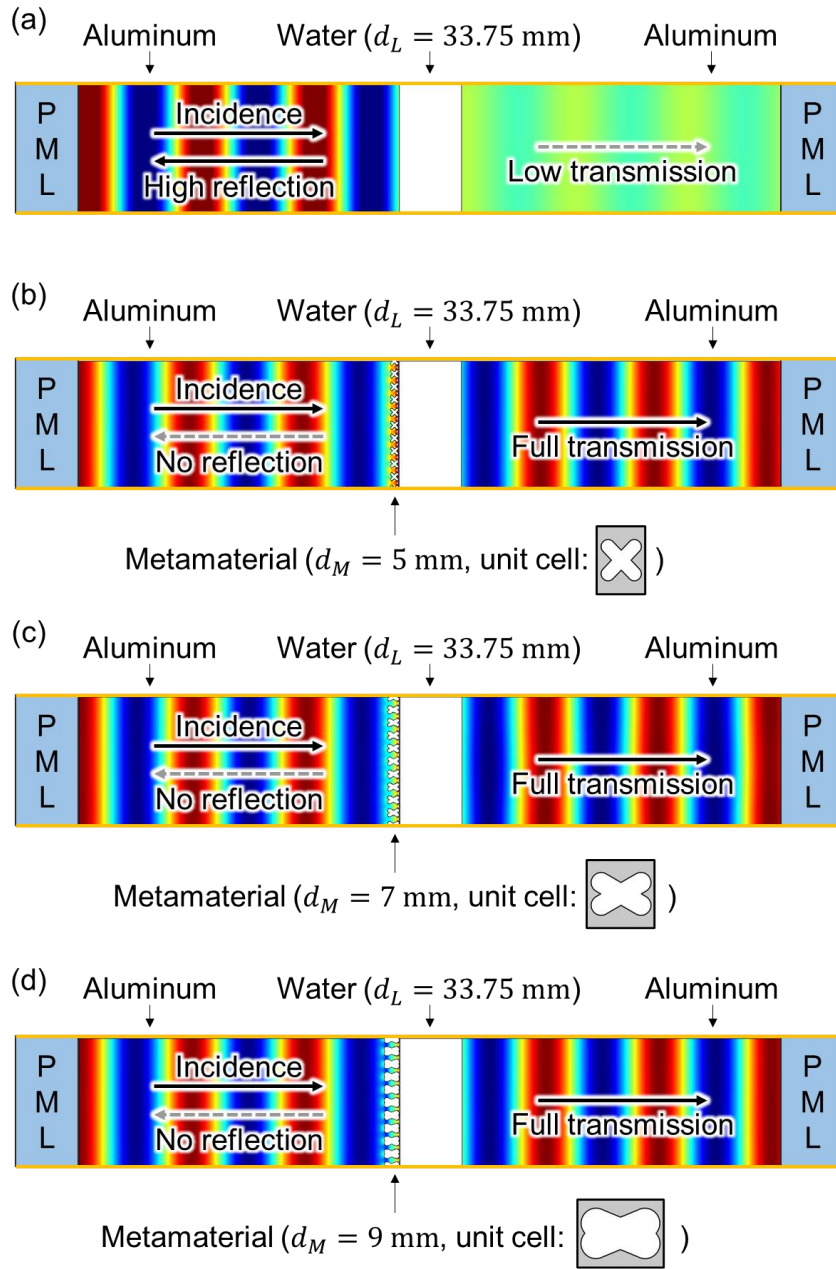


Fig. 4.1. Numerical simulation results (a) without metamaterials (only barrier) and with (b) 5mm, (c) 7mm, and (d) 9mm-thickness metamaterials.

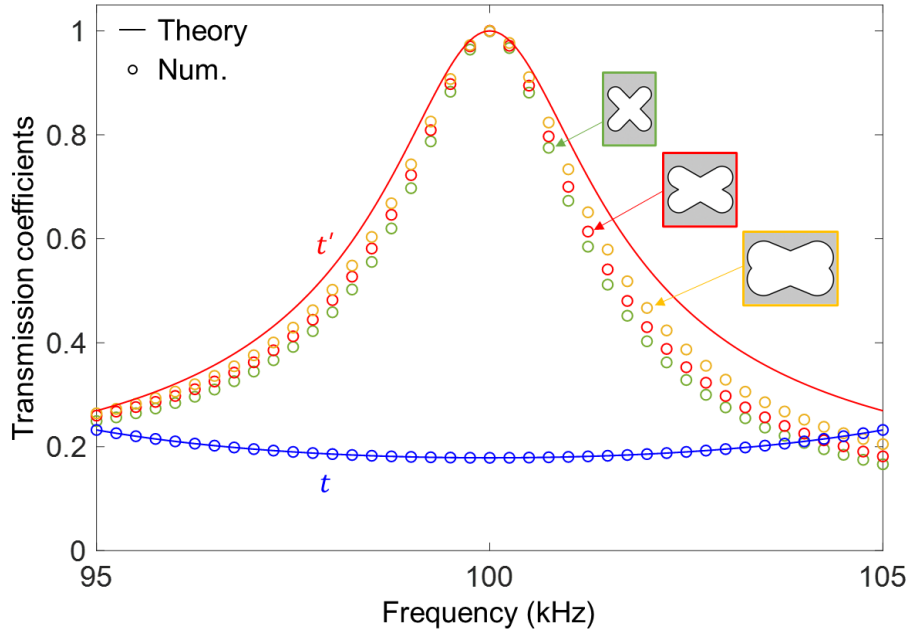


Fig. 4.2. Frequency response performance of the designed metamaterials. The solid line represents the theoretically calculated values, and the green (5mm), red (7mm), and yellow (9mm) circles indicate the performance of the designed metamaterials for each respective length.

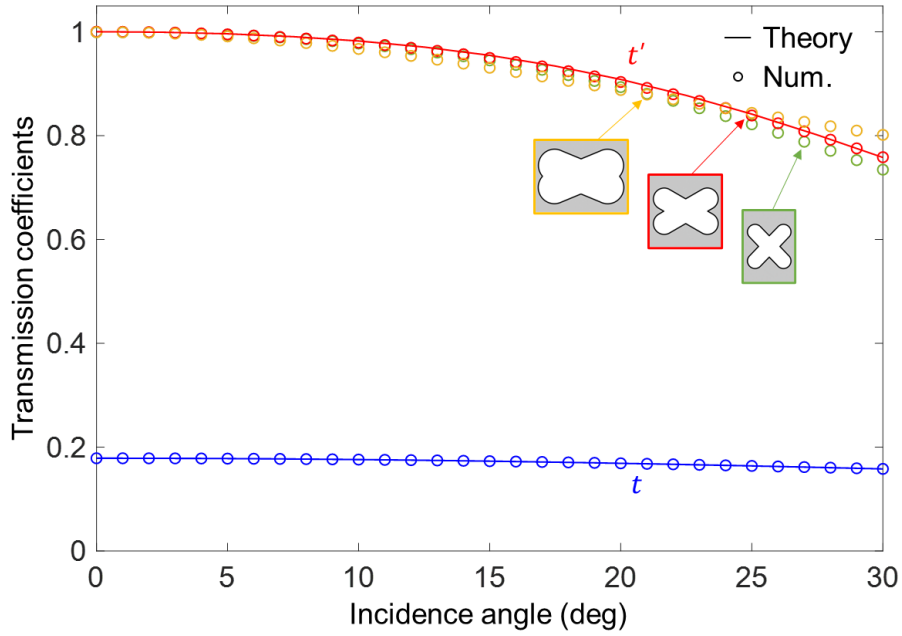


Fig. 4.3. Performance of the designed metamaterial at different incident angles. The solid line represents the theoretically calculated values, and the green (5mm), red (7mm), and yellow (9mm) circles indicate the performance of the designed metamaterials for each respective length.

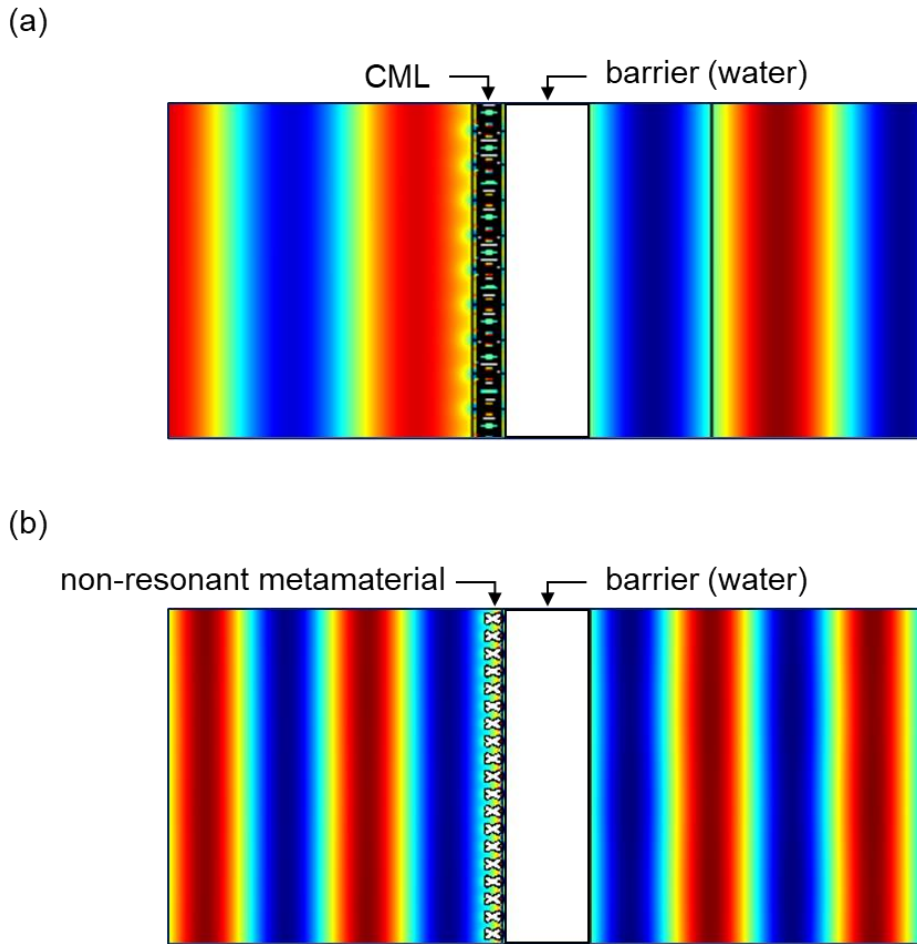
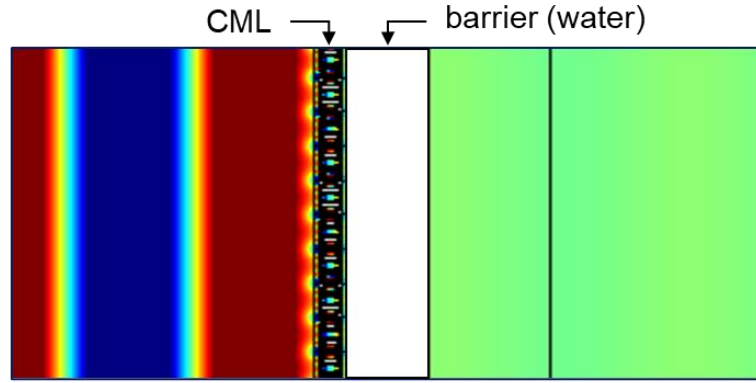


Fig. 4.4. Comparison of performance between CML and the proposed non-resonant metamaterial at each target frequency. (a) Barrier penetration at CML's target frequency of 55kHz. (b) Barrier penetration at the non-resonant metamaterial's target frequency of 100kHz.

(a)



(b)

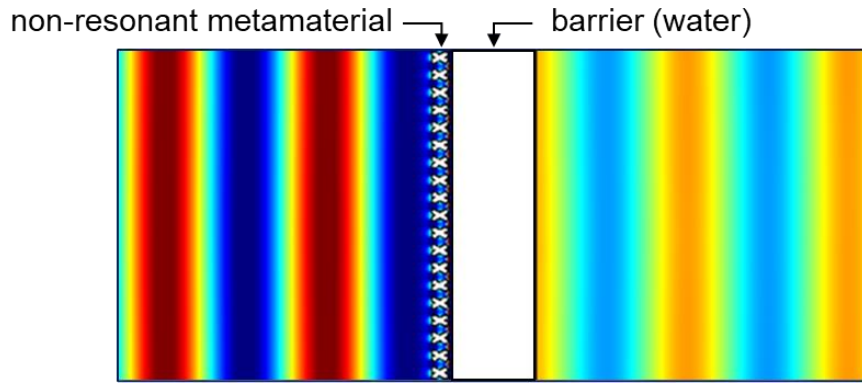


Fig. 4.5. Comparison of performance between CML and the proposed non-resonant metamaterial at offset frequencies. (a) Barrier penetration at 54kHz (1kHz offset) for CML. (b) Barrier penetration at 99kHz (1kHz offset) for the non-resonant metamaterial.

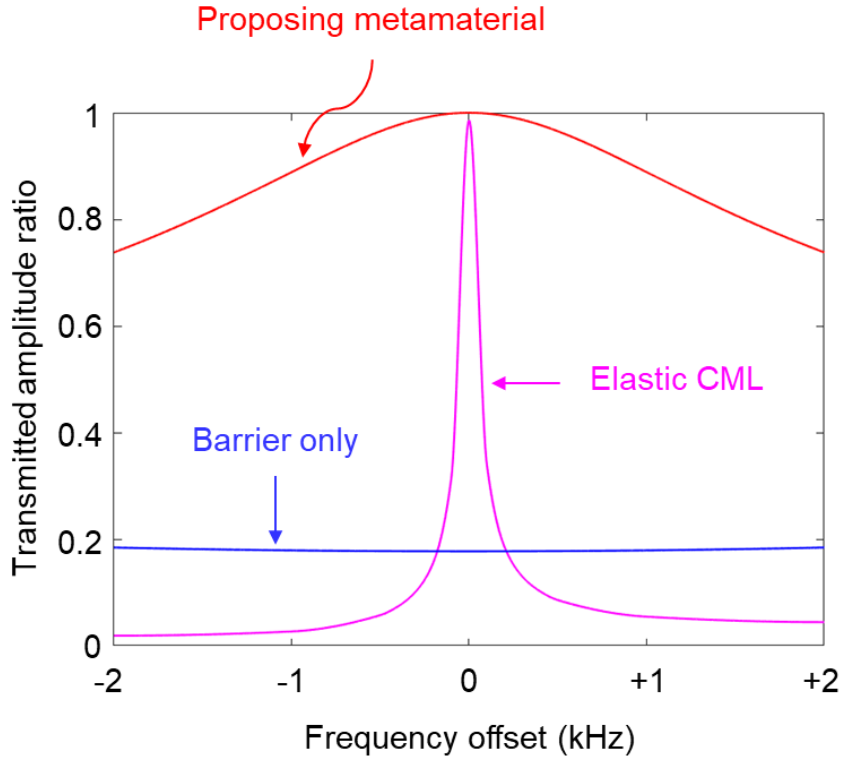


Fig. 4.6. Frequency sweep centered around the target frequency for the proposed non-resonant metamaterial (red), CML (magenta), and the case with only the barrier (blue).

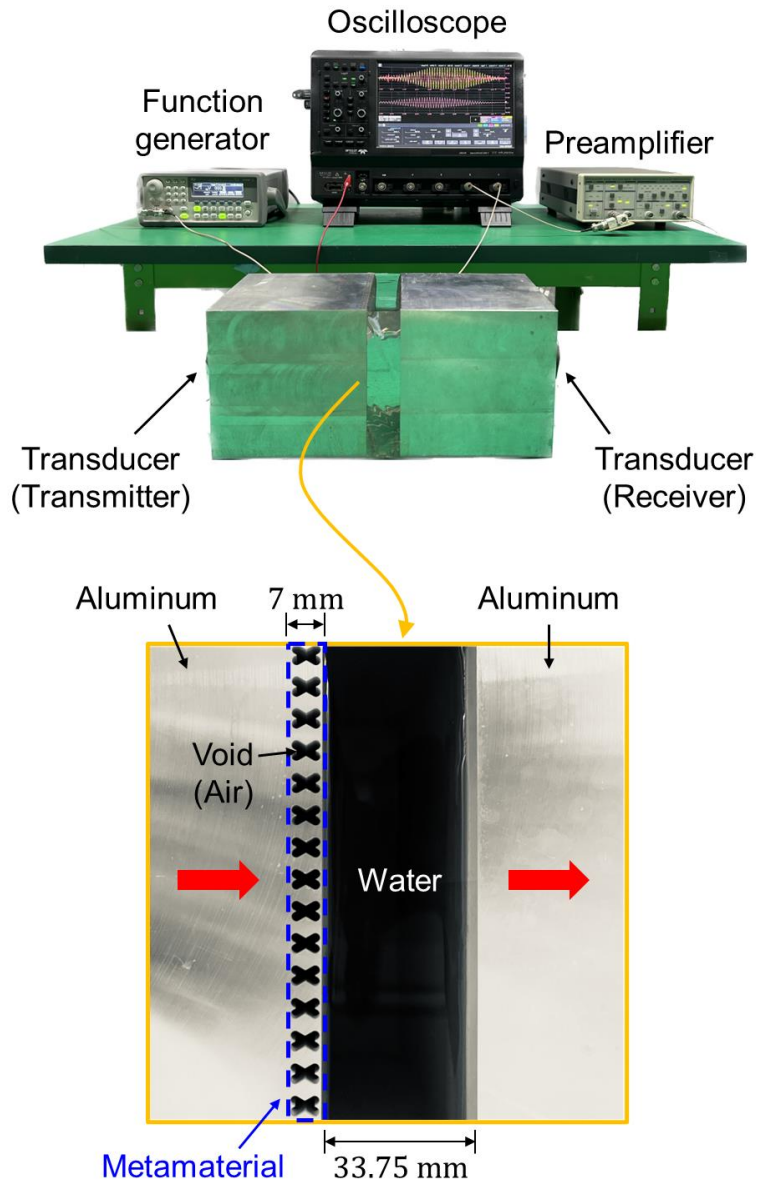


Fig. 4.7. Experimental setup with top view image of a test aluminum–water–aluminum block system including the barrier penetrating metamaterial.

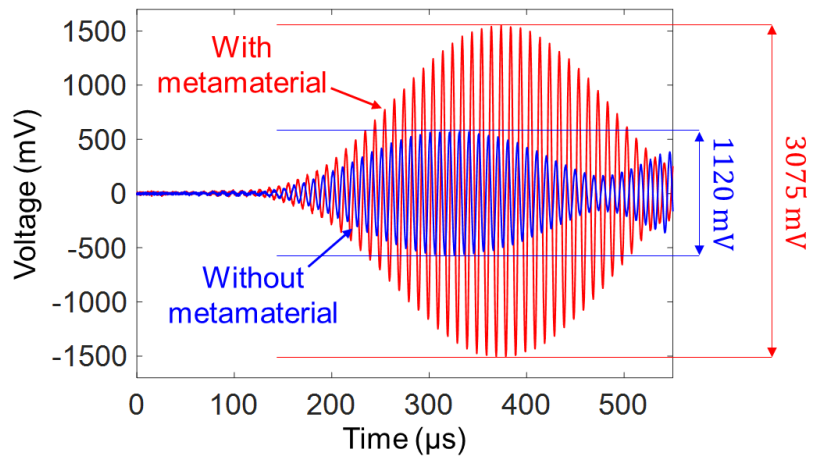


Fig. 4.8. Comparison of measured signals of with (red) and without (blue) the metamaterial.

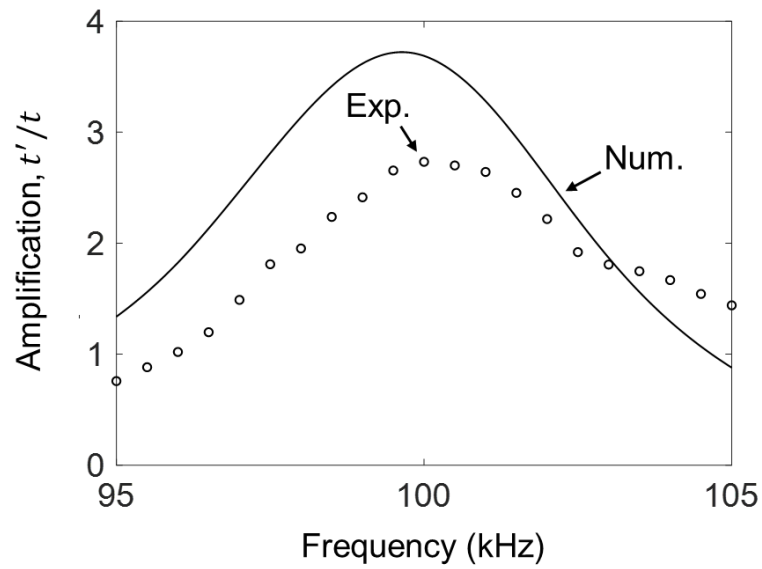


Fig. 4.9. Amplitude amplification with respect to the frequency. The numerical simulation results are indicated by lines, and experimental results are indicated by circles.

Chapter 5. Conclusion

Our study demonstrates that the insertion of a non-resonant barrier-penetrating metamaterial facilitates the flawless transmission of elastic waves incident on the barrier. We have ascertained the physical phenomena requisite for barrier penetration and the properties of metamaterials that enable full transmissions. The metamaterials with these specific properties were designed and subsequently validated through numerical simulations and experimentally. Moreover, we found that the proposed barrier penetration system using metamaterial layers is more robust to errors such as frequency and angle of incidence than previous studies using CML. This research has proved that the practical use of metamaterials for barrier penetration can be achieved by circumventing the experimental implementation challenges due to locally resonant structures in metamaterials and utilizing non-resonant structures instead. Additionally, we have demonstrated that the metamaterials enabling this process can be flexibly designed over a broad range of sizes while maintaining consistent performance. We anticipate that our findings will have a significant impact on industrial and medical applications where the transmission of high energy is critical. Our study focused on the case where the background medium is single; future research could explore the design of metamaterials for barrier penetration in cases involving dissimilar media.

Bibliography

- [1] Chen, H. T. *et al.* Active terahertz metamaterial devices. *Nature* **444**, (2006).
- [2] Arbabi, A., Horie, Y., Bagheri, M. & Faraon, A. Dielectric metasurfaces for complete control of phase and polarization with subwavelength spatial resolution and high transmission. *Nat Nanotechnol* **10**, (2015).
- [3] Xie, Y. *et al.* Wavefront modulation and subwavelength diffractive acoustics with an acoustic metasurface. *Nat Commun* **5**, (2014).
- [4] Kundtz, N. & Smith, D. R. Extreme-angle broadband metamaterial lens. *Nat Mater* **9**, (2010).
- [5] Oh, J. H., Seung, H. M. & Kim, Y. Y. Doubly negative isotropic elastic metamaterial for sub-wavelength focusing: Design and realization. *J Sound Vib* **410**, (2017).
- [6] Ahn, Y. K., Lee, H. J. & Kim, Y. Y. Conical Refraction of Elastic Waves by Anisotropic Metamaterials and Application for Parallel Translation of Elastic Waves. *Sci Rep* **7**, (2017).
- [7] Sreekanth, K. V. *et al.* Extreme sensitivity biosensing platform based on hyperbolic metamaterials. *Nat Mater* **15**, (2016).
- [8] Zhu, J. *et al.* A holey-structured metamaterial for acoustic deep-subwavelength imaging. *Nat Phys* **7**, (2011).
- [9] Shen, C. *et al.* Broadband Acoustic Hyperbolic Metamaterial. *Phys Rev Lett* **115**, (2015).
- [10] Kumar, R., Kumar, M., Chohan, J. S. & Kumar, S. Overview on

- metamaterial: History, types and applications. *Mater Today Proc* **56**, (2022).
- [11] Tian, X. *et al.* Wireless body sensor networks based on metamaterial textiles. *Nat Electron* **2**, (2019).
 - [12] Piao, C. *et al.* Ultrasonic flow measurement using a high-efficiency longitudinal-to-shear wave mode-converting meta-slab wedge. *Sens Actuators A Phys* **310**, (2020).
 - [13] Doucette, J. W. *et al.* Validation of a Doppler guide wire for intravascular measurement of coronary artery flow velocity. *Circulation* **85**, (1992).
 - [14] Hartley, C. J. & Cole, J. S. An ultrasonic pulsed Doppler system for measuring blood flow in small vessels. *J Appl Physiol* **37**, (1974).
 - [15] Abbate, A., Koay, J., Frankel, J., Schroeder, S. C. & Das, P. Signal detection and noise suppression using a wavelet transform signal processor: application to ultrasonic flaw detection. *IEEE Trans Ultrason Ferroelectr Freq Control* **44**, (1997).
 - [16] Lowe, M. J. Matrix Techniques for Modeling Ultrasonic Waves in Multilayered Media. *IEEE Trans Ultrason Ferroelectr Freq Control* **42**, (1995).
 - [17] Drinkwater, B. W. & Wilcox, P. D. Ultrasonic arrays for non-destructive evaluation: A review. *NDT and E International* vol. 39 Preprint at <https://doi.org/10.1016/j.ndteint.2006.03.006> (2006).
 - [18] Sarvazyan, A. P., Rudenko, O. V., Swanson, S. D., Fowlkes, J. B. & Emelianov, S. Y. Shear wave elasticity imaging: A new ultrasonic technology of medical diagnostics. *Ultrasound Med Biol* **24**, (1998).
 - [19] Lee, W. & Roh, Y. Ultrasonic transducers for medical diagnostic imaging. *Biomed Eng Lett* **7**, (2017).
 - [20] Allan, P. L. & McDicken, W. N. An Adaptive Weighted Median Filter

- for Speckle Suppression in Medical Ultrasonic Images. *IEEE Trans Circuits Syst* **36**, (1989).
- [21] Gururaja, T. R. Piezoelectrics for medical ultrasonic imaging. *American Ceramic Society Bulletin* **73**, (1994).
- [22] Perot, A. & Fabry, C. On the Application of Interference Phenomena to the Solution of Various Problems of Spectroscopy and Metrology. *Astrophys J* **9**, (1899).
- [23] Kobayashi, K. Complementary media of electrons. *Journal of Physics Condensed Matter* **18**, (2006).
- [24] Park, C. Il, Piao, C., Lee, H. & Kim, Y. Y. Elastic complementary meta-layer for ultrasound penetration through solid/liquid/gas barriers. *Int J Mech Sci* **206**, (2021).
- [25] Craig, S. R., Welch, P. J. & Shi, C. Non-Hermitian complementary acoustic metamaterials for lossy barriers. *Appl Phys Lett* **115**, (2019).
- [26] Lee, J., Kweun, M., Lee, W., Park, C. Il & Kim, Y. Y. Perfect transmission of elastic waves obliquely incident at solid-solid interfaces. *Extreme Mech Lett* **51**, (2022).
- [27] Lee, J., Park, J., Park, C. W., Cho, S. H. & Kim, Y. Y. Uni-modal retroreflection in multi-modal elastic wave fields. *Int J Mech Sci* **232**, (2022).
- [28] Zheng, M. *et al.* Non-resonant metasurface for broadband elastic wave mode splitting. *Appl Phys Lett* **116**, (2020).
- [29] Smith, D. R., Schultz, S., Markoš, P. & Soukoulis, C. M. Determination of effective permittivity and permeability of metamaterials from reflection and transmission coefficients. *Phys Rev B Condens Matter Mater Phys* **65**, (2002).
- [30] Chiffolleau, G. J. A., Steinberg, T. A. & Veidt, M. Reflection of structural waves at a solid/liquid interface. *Ultrasonics* **41**, (2003).

- [31] Tas, G. & Maris, H. J. Picosecond ultrasonic study of phonon reflection from solid–liquid interfaces. *Phys Rev B Condens Matter Mater Phys* **55**, (1997).
- [32] Plona, T. J., Pitts, L. E. & Mayer, W. G. Ultrasonic bounded beam reflection and transmission effects at a liquid/ solid-plate/liquid interface. *J Acoust Soc Am* **59**, (1976).
- [33] Veselago, V. G. THE ELECTRODYNAMICS OF SUBSTANCES WITH SIMULTANEOUSLY NEGATIVE VALUES OF ϵ AND μ . *Soviet Physics Uspekhi* **10**, (1968).
- [34] Yang, X., Kweun, M. & Kim, Y. Y. Monolayer metamaterial for full mode–converting transmission of elastic waves. *Appl Phys Lett* **115**, (2019).
- [35] Li, S., Shen, Z., Yin, W., Zhang, L. & Chen, X. 3D printed cross–shaped terahertz metamaterials with single–band, multi–band and broadband absorption. *Opt Mater (Amst)* **122**, (2021).
- [36] Huang, S. T., Hsu, S. F., Tang, K. Y., Yen, T. J. & Yao, D. J. Application of a terahertz system combined with an x–shaped metamaterial microfluidic cartridge. *Micromachines (Basel)* **11**, (2020).

Abstract (Korean)

비공진 장애물 투과 초음파 메타물질

김 기 현

서울대학교 대학원

기계공학부

파동이 진행할 때 장애물이 파동의 진행경로 상에 존재하는 경우, 그 계면에서 생기는 반사로 인해 투과율이 저하됩니다. 이러한 파동에서의 고유현상은 오랜 시간동안 탄성 초음파의 응용을 제한하는 요소로 자리매김해 왔습니다. 본 연구에서는 장애물을 넘어서 탄성 초음파를 원하는 위치로 완전 투과시키는 선구적인 메타물질 설계안을 제시합니다. 장애물을 넘어서 목표로 하는 지점까지 완전히 파동을 투과시키는 현상의 수학적 분석과 물리적 해석을 통하여 비공진형 메타물질의 설계를 통해 이 현상을 구현할 수 있음을 확인하고, 장애물 투과를 위한 비공진형 메타물질이 충족해야 할 이론적 전제조건들을 확인하고 설명합니다. 장애물 투과 물리현상의 이해를 통해 완전 투과 조건을 만족시키는 메타물질을 설계하였습니다. 제안된 메타물질의 유효성은 FEM 시뮬레이션을 통하여 수치적으로 검증되었습니다. 나아가, 알루미늄-물-알루미늄 시스템에서 초음파 실험을 통해 비공진형 장애물 투과 메타물질이 실현 가능성을 입증하였습니다. 이 연구의 결과는 장애물을 넘어서 수행하는 비파괴 검사 및 뇌 초음파 시스템과 같은 산업, 의료기기 분야 등에서의 새로운 대안을 제시합니다.

주요어 : 초음파, 탄성파, 장애물 완전투과, 페브리-페로 공진, 임피던스
정합

학번 : 2021-23094